RF-induced heating in tissue near bilateral DBS implants during MRI at 1.5 T and 3T: The role of surgical lead management

Laleh Golestanirad [a,b,*], John Kirsch [c], Giorgio Bonmassar [c], Sean Downs [c], Behzad Elahi [d], Alastair Martin [e], Maria-Ida Iacono [f], Leonardo M. Angelone [f], Boris Keil [g], Lawrence L. Wald [b,1], Julie Pilitsis [h,1]

[a] Department of Radiology, Feinberg School of Medicine, Northwestern University, Chicago, IL, USA
[b] Department of Biomedical Engineering, McCormick School of Engineering, Northwestern University, Evanston, IL, USA
[c] A. A. Martinos Center for Biomedical Imaging, Massachusetts General Hospital, Boston, MA, USA
[d] Department of Neurology, Mayo Clinic, Rochester, MN, USA
[e] Department of Radiology and Biomedical Imaging, University of California, San Francisco, CA, USA
[f] Division of Biomedical Physics, Office of Science and Engineering Laboratories, Center for Devices and Radiological Health, U.S. Food and Drug Administration, Silver Spring, MD, USA
[g] Department of Life Science Engineering, Institute of Medical Physics and Radiation Protection, Giessen, Germany
[h] Department of Neurosurgery, Albany Medical Center, Albany, NY, USA

ARTICLE INFO

ABSTRACT

Access to MRI is limited for patients with deep brain stimulation (DBS) implants due to safety hazards, including radiofrequency (RF) heating of tissue surrounding the leads. Computational models provide an exquisite tool to explore the multi-variate problem of RF heating and help better understand the interaction of electromagnetic fields and biological tissues. This paper presents a computational approach to assess RF-induced heating, in terms of specific absorption rate (SAR) in the tissue, around the tip of bilateral DBS leads during MRI at 64MHz/1.5 T and 127 MHz/3T. Patient-specific realistic lead models were constructed from post-operative CT images of nine patients operated for sub-thalamic nucleus DBS. Finite element method was applied to calculate the SAR at the tip of left and right DBS contact electrodes. Both transmit head coils and transmit body coils were analyzed. We found a substantial difference between the SAR and temperature rise at the tip of right and left DBS leads, with the lead contralateral to the implanted pulse generator (IPG) exhibiting up to 7 times higher SAR in simulations, and up to 10 times higher temperature rise during measurements. The orientation of incident electric field with respect to lead trajectories was explored and a metric to predict local SAR amplification was introduced. Modification of the lead trajectory was shown to substantially reduce the heating in phantom experiments using both conductive wires and commercially available DBS leads. Finally, the surgical feasibility of implementing the modified trajectories was demonstrated in a patient operated for bilateral DBS.

1. Introduction

Deep brain stimulation (DBS) of the thalamus or basal ganglia represents an effective technique to treat several major debilitating movement disorders including Parkinson's disease, essential tremor, and dystonia (Limousinet al, 1995; Benabid, 2003; Benabid et al., 2009; Kumar et al., 1999; Ostrem and Starr, 2008; Vercueilet al, 2001; Hubble et al., 1996; Blomstedt et al., 2007; Flora et al., 2010). While decades have passed since the inception of DBS and its clinical utility has grown

exponentially, its underlying therapeutic mechanisms of action remain controversial. Uncertainties remain about which circuits are affected, which exact fiber bundles need to be targeted, and the most efficient stimulation protocol (McIntyre et al., 2004a, 2004b). The meticulous use of neuroimaging, both for target verification and for post-operative monitoring of treatment-induced changes in the functional connectivity of affected brain networks is essential to interpret clinical outcomes, test new hypotheses, and design enhanced therapeutic protocols. Due to its superb soft tissue contrast and high-resolution visualization of the brain
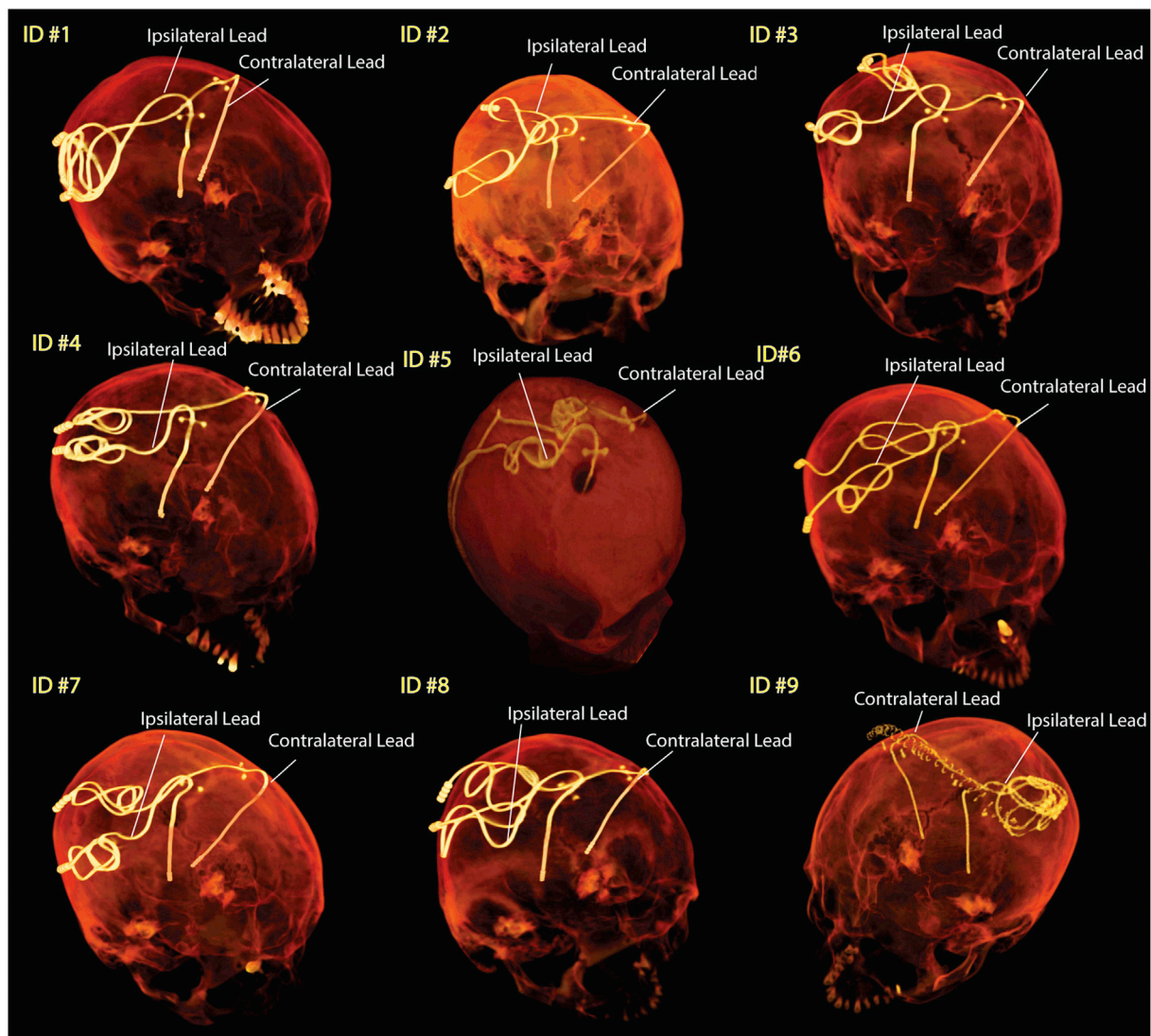

Fig. 1. Post-operative CT images of patients with bilateral DBS leads. The ipsilateral and contralateral labels are with respect to the system IPG.

anatomy, magnetic resonance imaging (MRI) is excellently poised as a non-invasive imaging tool to address open questions regarding DBS targeting and mechanism. Unfortunately, the interaction between the MRI scanners and implanted DBS devices can result in restricting safety hazards that limit the accessibility of MRI for this patient population (Panych and Madore, 2018).

Since first reports of harmful interaction between MRI environment and implantable electronic devices in 1989 (Pavliceket al, 1983) significant improvement has been made in design and manufacturing of medical implants. Such improvements include for example, reduction of ferromagnetic material to reduce the risk of device dislodgement due to static magnetic fields (Shellock et al., 2007), and enhanced programming to reduce the risk of device malfunction due to MRI gradient effects (Sommeret al, 2006). The major restriction of present MRI technology for DBS imaging is the interaction of radiofrequency (RF) fields and implanted electrodes. The coupling of RF fields with long conductive leads induces electric currents on lead wires, which increase energy absorption in the tissue surrounding the lead electrodes. Such high energy may in turn generate excessive temperature rise and possible tissue damage (Rezaiet al, 2005; Rezaiet al, 2004). To limit such risks, the conditions under which patients with DBS are indicated for MRI are restrictive. For example, only static magnetic field of 1.5 T is recommended, and applied pulse sequences need to have limited RF power (in

terms of either reduced SAR or B_1 rms). Such limitations exclude for example, patients in centers that have only 3T MRI systems and current state-of-the-art MRI multi-transmit technology is absolutely contra-indicated as well (Medtronic, 2017). Although recent developments in introducing patient-adjustable MRI technology (Golestaniradet al, 2017; Golestanirad et al., 2017) and parallel transmit techniques (McElcheran et al., 2014, 2015, 2017) have shown promising results for DBS imaging, such advancements are still far from clinical application. Practical and easy-to-implement lead management strategies that mitigate the risk of RF heating are thus, highly desirable.

RF heating is a complex phenomenon with several interplaying factors including the anatomy of the patient, imaging landmark, frequency, geometry, and type of the RF transmitter, as well as the topology of the implant (Matteiet al, 2008a; Calcagniniet al, 2008; Nordbecket al, 2009; Nordbecket al, 2008). Phantom experiments have established that the lead trajectory has a substantial effect on the SAR in the tissue (Baker et al., 2005; Shrivastavaet al, 2010; Golestanirad et al., 2016a), yet almost nothing is known about the variation of RF heating as a function of lead implantation path in real patient populations. In this study, a computational approach is applied to assess the SAR in the tissue around the tip of DBS leads in patient-specific computational models. CT-data from 9 patients were used to generate computational models of real-istic lead trajectories and RF heating was studied using finite-element
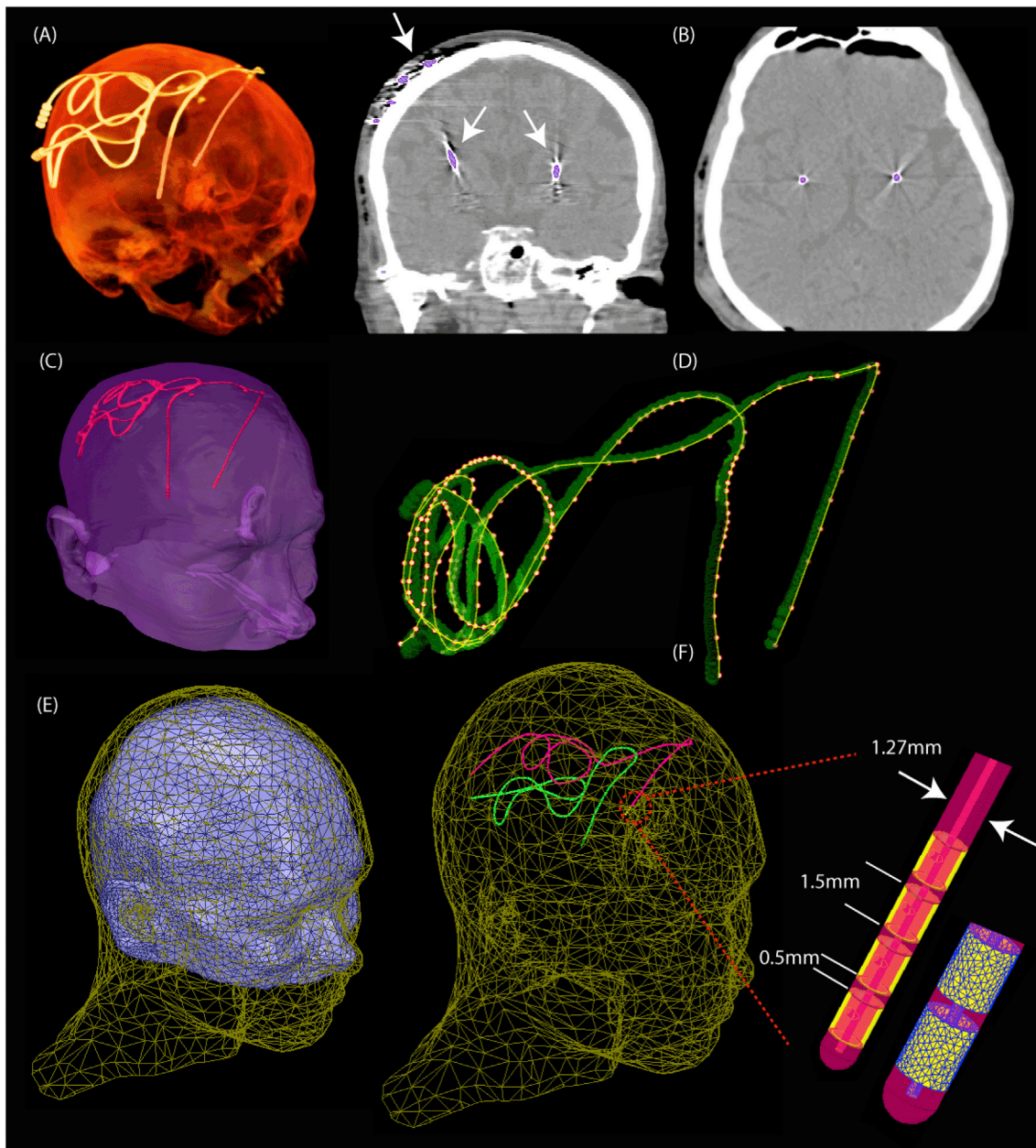
Fig. 2. Steps of image segmentation and lead model construction. (A) 3D view of the CT image of a patient (B) Threshold mask covering the center of hyper dense lead artifact (C) Preliminary 3D surfaces of patient's head and lad trajectories constructed in Amira. (D) Lead trajectories reconstructed in Rhino3D. Adjustments were made to assure there was at lead 1.27 mm gap between overlapping segments. (E) Patient's head aligned with the homogeneous MIDA model. (F) Details of lead structure and mesh in HFSS.

simulations. Results were used to optimize the routing of DBS leads to reduce the heating.

In what follows, the conventional DBS implantation procedure and typical features of ipsilateral and contralateral leads are discussed; details of finite element modeling and SAR calculation at the tip of realistic lead trajectories inside an RF head coil and an RF body coil at two frequencies and different feed positions are presented; a new metric to predict the SAR from relative orientation of the lead with respect to the incident electric field is introduced; results of phantom experiments with implanted wires and commercially available leads are presented; modified implantation paths that reduce the risk of RF heating are examined, and finally, surgical feasibility of implementing MRI-friendly DBS trajectories is demonstrated. The paper concludes with a discussion of safety considerations and a brief description of future work to devise surgical DBS guidelines that reduce the risk of post-operative MRI examinations.

1.1. SAR in contralateral vs. ipsilateral DBS leads: patient-derived simulations at 1.5 T and 3 T

When it comes to the RF safety of elongated implants, the position and configuration of the lead are shown to have a substantial effect on the SAR distribution (Matteiet al, 2008a; Calcagniniet al, 2008; Nordbecket al, 2009; Nordbecket al, 2008). Commercial DBS leads come with a prefixed length which is usually longer than needed. In conventional DBS surgery, surgeons tend to keep the extra portion of lead extension at the level of cranium to avoid positioning against the soft tissue in the neck. As a result, leads are looped several times in a random pattern, leading to a substantial patient-to-patient variation in their routing (see Fig. 1). In most cases where bilateral leads are implanted, a two-channel implanted pulse generator (IPG) is positioned unilaterally in the chest to stimulate both leads. In such cases, ipsilateral and contralateral leads follow different
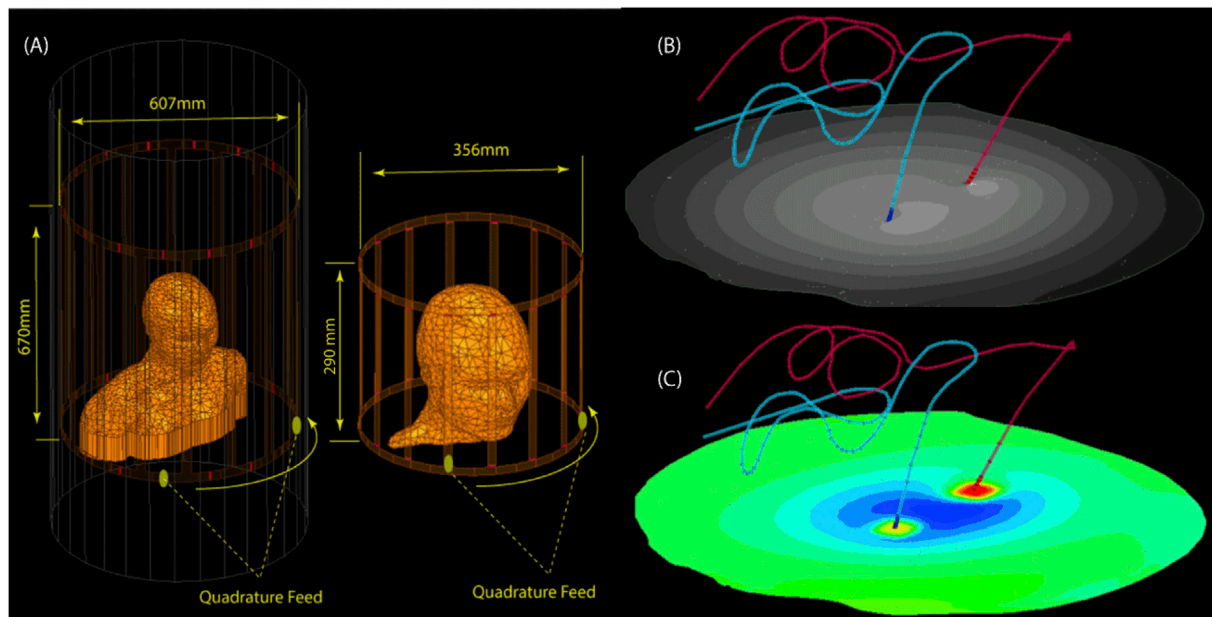
Fig. 3. (A) position of paitent body in head and body coils. (B) the B_1+ and (C) 1gSAR calculated on an axial plane passing through electrode contacts.

geometrical paths. Fig. 1 shows post-operative CT images of nine patients with bilateral leads. As shown, contralateral leads which exit the surgical burr-hole at a further point from the IPG are first tunneled to the IPG side along a medio-lateral straight path. The ipsilateral leads in contrast, are first looped right at the burr-hole (complete or half-loop) before being routed toward the neck. Antenna theory indicates that the source of induced currents along conductive leads is the tangential – rather than perpendicular - component of the incident electric field along the lead trajectory (E_{tan}) (Nordbecket al, 2008; Park et al., 2007). Specifically, the integral of E_{tan} along the lead generates a virtual distributed voltage source across the entire lead length, inducing RF currents on the wires that in turn give rise to scattered electric fields in the tissue at the vicinity of the exposed tip. These scattered secondary fields are responsible for amplifying the energy absorption in the tissue; if the energy increase is not counterbalanced by the tissue thermoregulatory system, temperature increase, and possible thermal damage can occur. Because ipsilateral and contralateral leads have different orientations with respect to the incident electric field E_{tan}, we hypothesize that the SAR at the tip of these lead groups will be significantly different. Specifically, we hypothesize that contralateral leads exhibit a higher SAR due to the strong coupling of the initial extracranial segment of the lead with the incident electric field. Section 2 outlines the details of numerical modeling and results of SAR amplification around tips of ipsilateral and contralateral DBS leads in nine patient-specific models. Analysis was performed at both 64MHz/1.5T and 127 MHz/3T and with both transmit head coils and body coils. Section 3 describes phantom experiments with wire implants as well as Medtronic lead models 3389 and 3387 and demonstrates modified lead trajectories that substantially reduce the heating at the tip. Finally, section 4 describes an example of the clinical application of modifying lead trajectory as suggested by simulation results. It is important to note however, that the present study is limited to the assessment of DBS leads in isolation, i.e., prior to their attachment to the lead extensions and/or the IPG. Further investigation is required to establish whether the data presented here applies to the fully implanted systems.

2. Numerical modeling

2.1. Realistic lead models

Intraoperative CT images of nine patients who had undergone bilateral DBS implantation at Massachusetts General Hospital and Albany

Medical Center were used for modeling (Fig. 1). CT images of patients 1–4 and 6–8 had 0.4 mm × 0.4 mm × 0.6 mm voxel resolution whereas those of patients 5 and 9 had 0.6 mm × 0.6 mm × 1.2 mm voxel resolution. Amira 5.3 (Thermo Fisher Scientific, Waltham MA) was used for image segmentation and construction of the preliminary 3D surface of the leads. First, a thresholding mask was applied to select the hyper dense DBS lead from CT images using Amira's segmentation module (Fig. 2B). Threshold values were selected manually on a case-by-case basis such that the resulting mask covered the center of the artifact but not the surrounding tissue such as bone. Labels were smoothed with a Gaussian filter (3×3 pixel size) and the resulting mask was used to generate preliminary 3D surfaces of the lead trajectories (Fig. 2C). 3D lead surfaces were exported to a CAD tool (Rhino3D®, Robert McNeal and Associates, Seattle, WA) in which lead trajectory lines were manually reconstructed. Adjustments were made as necessary to ensure there is more than 1.27 mm gap between overlapping segments, so that reconstructed lead do not intersect itself after addition of the insulation layer (Fig. 2D). The reconstructed trajectory lines were exported to ANSYS HFSS where models of electrode contacts, core, and insulation were constructed around them (Fig. 2F). A total of 18 leads were modelled. Models were composed of four cylindrical contacts (outer diameter = 1.27 mm, wall thickness = 150 μm), connected through a solid straight central core (diameter = 260 μm) and embedded in polyurethane insulation (diameter = 1.27 mm, $\sigma = 10^{-10}$ s/m, $\varepsilon_r = 3.5$ (Elwassif et al., 2006)). Electrode contacts were made of 90%:10% platinum-iridium (Pt:Ir, $\sigma = 4 \times 10^6$ S/m) positioned 0.5- mm apart. The reconstructed lead models were incorporated either into a homogeneous version of the anatomically-precise head model "MIDA" (Iaconoet al, 2015) (for simulations with transmit head coil) or a homogeneous head and torso model (for simulations with a transmit body coil). Anatomical models were assigned electrical properties equal to the average brain tissue ($\sigma = 0.49$ S/m, $\varepsilon_r = 66$ (Gabriel et al., 1996a; Gabriel et al., 1996b)). A triangulated surface of the patient's head was generated from CT images and used for rigid alignment of the lead inside the body.

2.2. MRI RF coil models and electromagnetic simulations

Electromagnetic simulations were implemented in ANSYS Electronics Desktop (HFSS 16.2, Designer, ANSYS Inc., Canonsburg, PA). Numerical models of two high-pass birdcage body coils (620 mm length, 607 mm

Table 1

Mesh statistics for a typical simulation. The total number of tetrahedral element including the coil and the region surrounding the model was 2006158.

	Mesh elements	Min edge length	Max edge length
Left lead core	50052	0.008 mm	0.5 mm
Right lead core	49150	0.008 mm	0.5 mm
Left lead insulation	140149	0.005 mm	2.5 mm
Right lead insulation	136927	0.02 mm	2.5 mm
Body	783910	0.06 mm	12 mm

diameter) and two low-pass transmit head-only coils (292 mm length, 356 mm diameter) were implemented and tuned to their respective Larmor frequencies - 64 MHz (1.5 T proton imaging) and 127 MHz (3 T). A quadrature excitation was implemented by feeding the coils at two ports on the bottom end-ring that were 90° apart in position and phase (Fig. 3A).

The effect of the phase distribution of the transmit field on the RF heating of conductive wires has been established in earlier studies (Yeung et al., 2002). Recently, it was demonstrated that the position of the feed of quadrature birdcage coils with respect to the body has a non-negligible effect on the heating of elongated implants (Lucanoet al, 2018). Therefore, for each patient model coils were rotated around the head with 45° increments to account for the variability of incident electric field orientation with respect to the leads.

A total of 288 simulations were performed (nine patient models × four RF transmit coils × eight different feed positions). For each simulation, the input power of the coil was adjusted to produce a spatial mean of $B_1^+ = 2\,\mu T$ on a transverse plane passing through the center of the coil (Fig. 3B). This is in line with the current DBS MRI guideline which states the maximum B_1^+rms should not exceed $2\,\mu T$ for safe use of the device at 1.5 T (Medtronic, 2017). Hence, reporting the associated local SAR values for this RF level are relevant. 1g-averaged SAR was calculated according to IEEE STD P1528.4 recommendation (P1528.4™/D1.0,Recomm, 2014), using the built-in SAR calculation module in ANSYS HFSS. The maximum of 1g-averaged SAR in a $2\,cm \times 2\,cm \times 2\,cm$ cubic area around the tip of each lead was calculated and reported as *MaxSAR1g* (Fig. 3C).

2.3. Numerical convergence

At the start of each simulation, ANSYS HFSS was set to follow an adaptive mesh scheme. The algorithm started with a user-controlled initial tetrahedral mesh which forced a fine resolution on the DBS lead

(maximum tetrahedron edge < 0.5 mm). The adaptive algorithm then refined the mesh by 30% between each two iterative simulations. At each step, the maximum change in the magnitude of S-parameters, ΔS, was defined as $\Delta S = Max_{ij}|S_{Nij}-S_{N-1ij}|$, where i and j cover all matrix entries and N represents the iteration number. The adaptive simulation continued until the threshold of $\Delta S < 0.01$ was reached. All simulations converged after N = 4 adaptive passes. Details of mesh statistics for a typical simulation are given in Table 1.

2.4. The incident electric field

To better understand how the orientation of the incident electric field with respect to lead trajectory affects SAR at the tip, we calculated the incident E_{tan} along the length of lead trajectories. To do this, simulations were performed without lead being present for both head coils and body coils and at both 64 MHz and 127 MHz. Polylines representing lead trajectories were imported to HFSS, and their unit tangent vectors were extracted using HFSS Field Calculator module. $E_{tan}(t)$ at each point along the length of the lead was calculated as:

$$E_{tan}(t) = \vec{E}(t) \cdot \hat{a} \tag{1}$$

Here $\vec{E}$ is the incident electric field and $\hat{a}$ is a unit vector tangential to the lead path. Fig. 4A shows all 18 lead trajectories superimposed in the head model with blue lines representing ipsilateral leads and red lines representing contralateral leads. Green arrows in Fig. 4B show the incident electric field $\vec{E}$ at a certain time point along ipsilateral and contralateral leads of a representative patient (Patient 2). Fig. 4B also shows the calculated $E_{tan}(t)$ along the length of the leads overlaid as a color field on top of lead trajectories for a specific time point. As it can be observed, E_{tan} has a distinct value at any point along the length of the lead. Also note that the magnitude of E_{tan} as calculated in (Limousinet al, 1995) is a function of time as the orientation of the electric field changes as the field rotates. The evolution of the $E_{tan}(t)$ along the length of ipsilateral and contralateral leads of Fig. 4 at five different time points through the cycle are given in the Supplementary Figure S1.

To have a metric that allows comparison of different trajectories, we calculated the peak-to-peak value of the induced voltage along the first 8 cm of the extracranial portion of each lead as:

$$V_{8cm}pp = \int_P^Q E_{tan}(t)\,dl\Big|_{peak-to-peak} \tag{2}$$

The integration in (Benabid, 2003) is taken between the point P (i.e.,
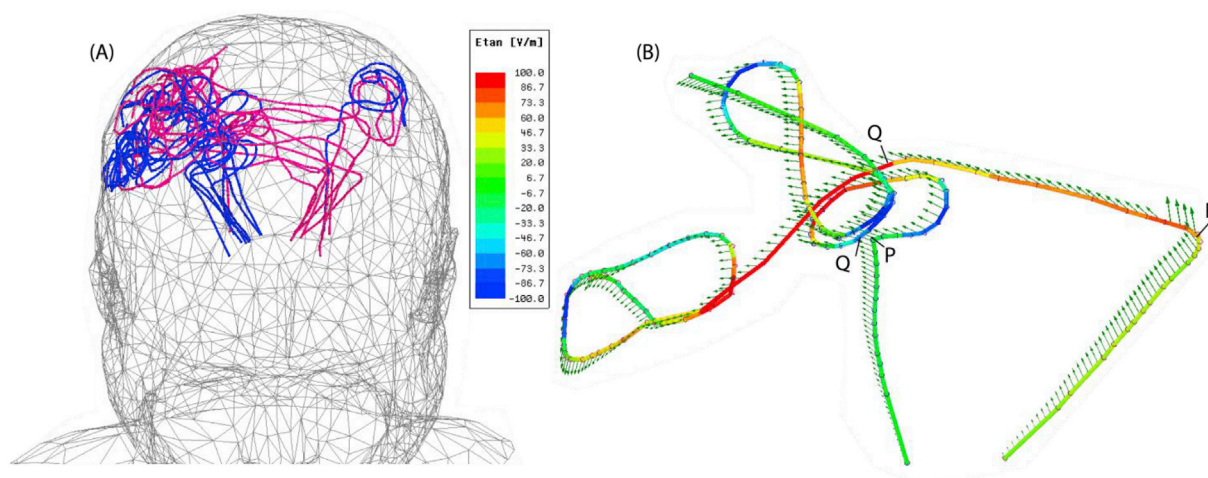
Fig. 4. (A) Trajectories of ipsilateral and contralateral leads superimposed in one head model. (B) Incident electric field (green arrows) and E_{tan} (color field) along the trajectory of ipsilateral and contralateral leads in Patient 2. Points P and Q show the limits of the initial segment over which the induced voltage V_{8cm} in equation (Benabid, 2003) was calculated. The evolution of E_{tan} at different time points through the cycle is given in Supplementary Figure S1.
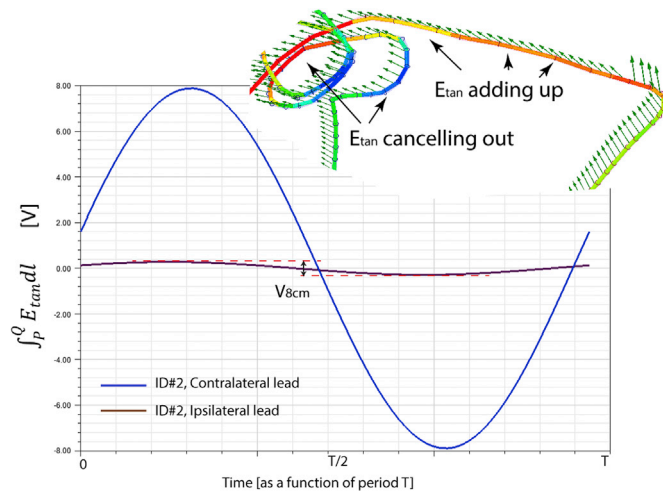
Fig. 5. Time evolution of the induced voltage over the first 8 cm segment of contralateral and ipsilateral leads in Patient 2.

lead exit point from the skull), and point Q 8 cm further along the extracranial portion of the lead. This is the portion of the lead where ipsilateral and contralateral trajectories follow substantially different paths, with contralateral leads following a straight path to be tunneled toward the IPG side, and ipsilateral leads being looped at their exit point on the skull (see Fig. 4A and Figure S1 in the Supplementary Material).

Fig. 5 shows the time evolution of $\int_P^Q E_{tan} dl$ for contralateral and ipsilateral leads of patient 2.

2.5. Simulation results

Fig. 6 gives the result of the single patient analysis, reporting the mean values of *MaxSAR1g* (averaged over feed positions) at each resonant frequency (64 MHz, 127 MHz) and for both head and body coils. As expected, there was a substantial difference between *MaxSAR1g* at the tip of contralateral vs. ipsilateral leads, with the latter being substantially lower. The effect was persistent in all patients and was consistent over different coil types and resonant frequencies. Specifically, the change of feed position did not alter the balance between contralateral and
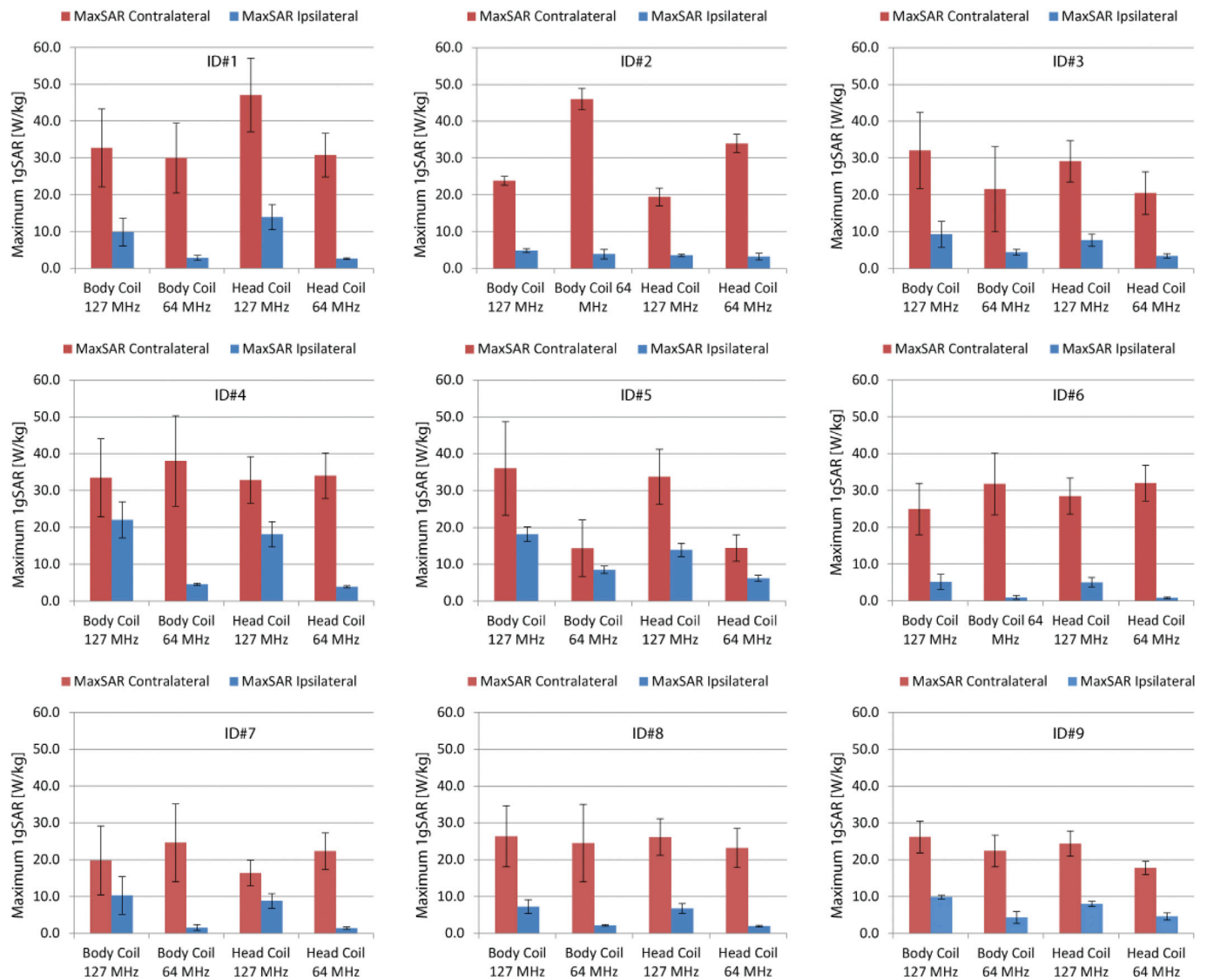

Fig. 6. MaxSAR1g for contralateral and ipsilateral leads in patients 1–9 for RF exposure at 64 MHz and 127 MHz with transmit head coil and transmit body coil.

Table 2
Mean of MaxSAR1g± standard deviation for head and body coils at 64 MHz and 127 MHz.

	MaxSAR1g Contralateral	MaxSAR1g Ipsilateral
Body Coil 127 MHz	28.4 ± 5.3	10.7 ± 5.7
Body Coil 64 MHz	28.1 ± 9.5	3.7 ± 2.2
Head Coil 127 MHz	28.6 ± 8.9	9.5 ± 4.7
Head Coil 64 MHz	25.4 ± 7.4	3.1 ± 1.6

ipsilateral SAR (not apparent in Fig. 6). This means that in all patient models when the coil was rotated around the head, ipsilateral SAR remained lower than the contralateral SAR.

Table 2 summarizes the results of group analysis on patients 1–9, reporting the mean of *MaxSAR1g* for each coil type and resonant frequency. At 64 MHz, the mean *MaxSAR1g* of contralateral leads was approximately 7 times higher than that of ipsilateral leads. At 127 MHz, the mean *MaxSAR1g* of contralateral leads was approximately 3 times higher than that of ipsilateral leads.

2.6. Interpretation of the results in the light of lead trajectory features

The SAR results presented here can be explained in the light of the specific features of lead trajectories, considering topological differences in the routing of ipsilateral vs contralateral leads. In all our patients, a single IPG was used to stimulate both left and right DBS leads. In eight patients (1–8), the IPG was implanted in the right pectoral region. In these patients, the right DBS lead was labeled as ipsilateral and the left lead as contralateral. One patient (Patient 9) had the IPG implanted in the left pectoral region for which the right DBS lead was labeled as contralateral and the left DBS leas as ipsilateral. A close examination of the tangential component of incident E field shows that E_{tan} adds up constructively over the initial extracranial straight segment of contralateral leads whereas its effect is mostly canceled out along the initial loop in ipsilateral leads. This effect is particularly pronounced in cases that demonstrated the larger difference between contralateral and ipsilateral SAR. An example is given for Patient 2 in Fig. 5.

Fig. 7 gives the scattering plots and correlation coefficients of *MaxSAR1g* vs V_{8cm} for all 18 leads. As it can be observed, there is a strong correlation between the induced voltage along the initial segment of the lead and the SAR amplification at the tip. This suggests that modifying the routing of contralateral leads in a way that reduces the induced voltage may also reduce the SAR amplification at the tip. Specifically, we hypothesize that introducing a looped section in the initial extracranial segment of the lead (right out of burr-hole) reduces the heating at the tip, as this part of the lead is exposed to the maximum tangential E field. The
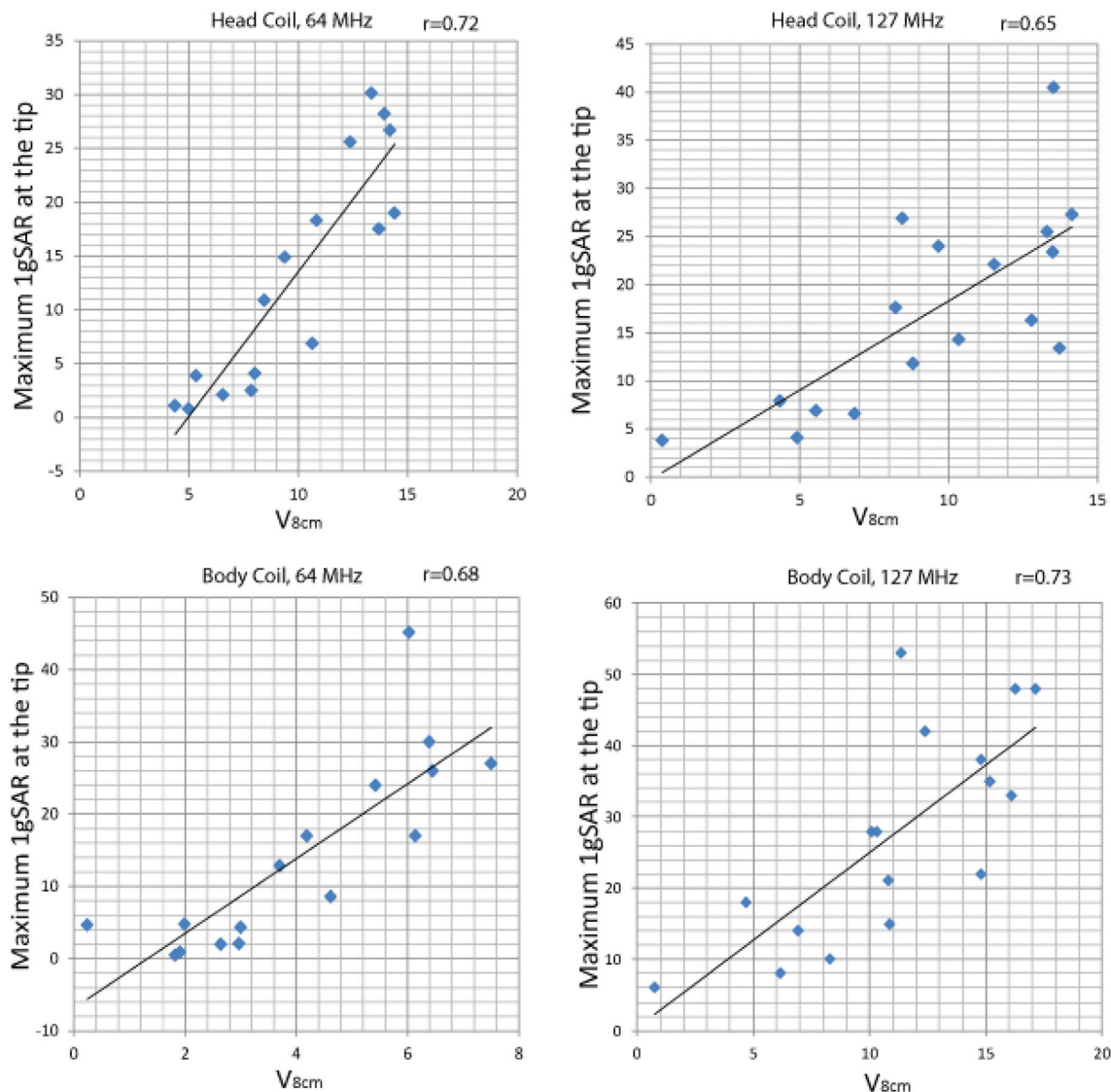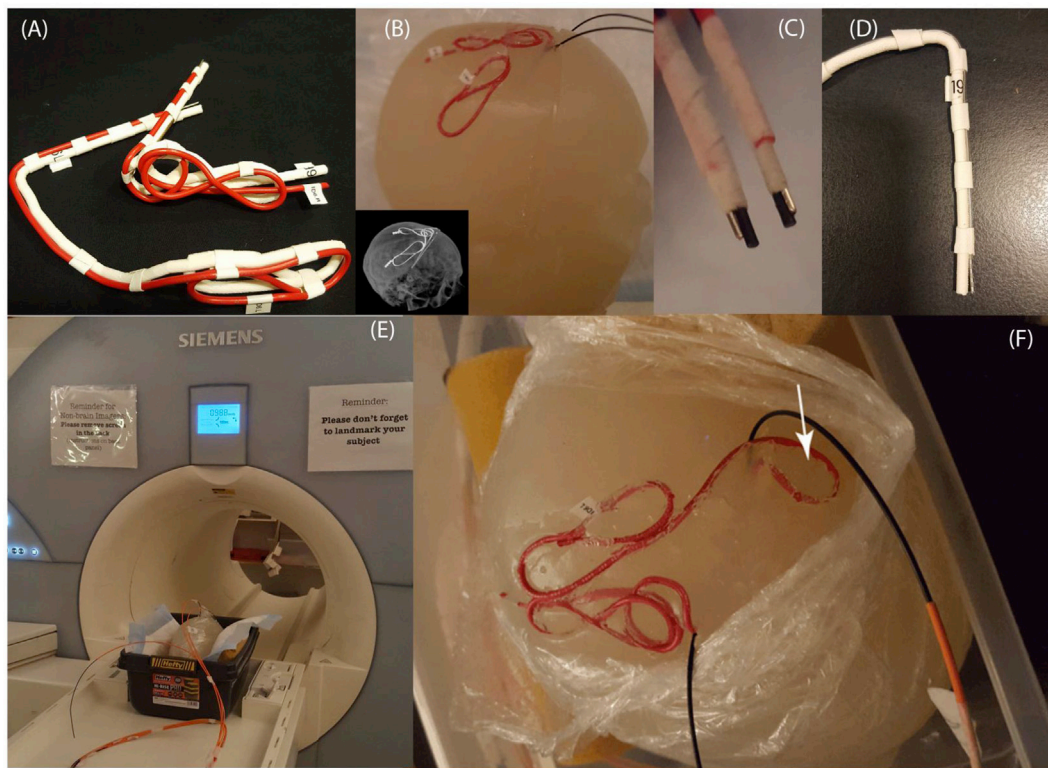

Fig. 7. Scattering plots and correlation coeffecients of V_{8cm} and *MaxSAR1g* for different body coils and at different resonant frequencies.

Fig. 8. (A) 3D printed DBS lead phantoms used as a guide to shape wires in the form of patient-derived trajectories. (B–E) Generic metallic wires and commercially available leads (Models 3387 and 3389, Medtronic Inc., Minneapolis) implanted into semi-solid anthropomorphic head phantoms for MRI at 1.5 T and 3T. (F) Modified contralateral trajectory of Patient 2 with an extracranial loop added at the surgical burr-hole.

next Section outlines the phantom experiments to verify this hypothesis.

3. Reducing the SAR through modification of the lead trajectory: phantom experiments at 1.5 T and 3 T

3.1. Phantom and lead construction

We tested the hypothesis that modification of the initial extracranial segment of the contralateral lead helps to reduce the SAR at its tip, by performing phantom experiments on lead models of Patient 2 which showed the largest difference between ipsilateral and contralateral *MaxSAR1g*. Digital models of the leads were 3D printed out of polycarbonate plastic (4 mm diameter) and were used as a guide. Two pieces of insulated wire (Ga 14, 40 cm long, 1 cm exposed tip) were shaped around 3D printed guides to follow the ipsilateral and contralateral trajectories (Fig. 8A). Semi-solid anthropomorphic head phantoms were constructed from agar-doped saline solutions with electrical and thermal properties mimicking biological tissues ($\varepsilon_r \cong 70$, $\sigma \cong 1$ S/m, $C_p = 4150$ J/kg°C). Phantom recipe and construction method is given in previous studies (Golestanirad et al., 2017). Leads were implanted into the gel phantom following the entrance point, angle, and trajectories as observed from CT images of the patient (Fig. 8B). To investigate the effect of trajectory, a modified contralateral lead trajectory was prepared where a single loop was introduced at the initial segment of the wire (Fig. 8F). Experiments were also repeated with commercially available DBS leads (Models 3387 and 3389, Medtronic, Minneapolis MN) (Fig. 8D).

3.2. RF exposure and temperature measurements

The temperature was recorded using fluoroptic temperature probes (OSENSA, BC, Canada) secured at the exposed tip of the leads (Fig. 8C). Experiments were performed at a 1.5T Magnetom Avanto system and a 3T TIM Trio system (Siemens Healthineers, Germany). Gradient coils

Table 3
Characteristics of the RF pulses.

Frequency	Flip Angle	Duration	TR	Patient weight entered	Whole-body SAR
64 MHz	200°	166 s	6.5 ms	68 kg	3.7 W/kg
127 MHz	250°	148 s	28.9 ms	68 kg	4 W/kg

Table 4
Temperature rise in the gel at the tip of ipsilateral and contralateral leads for RF exposures of Table 3.

Temperature rise [°C]	1.5 T (64 MHz)		3 T (127 MHz)	
	Ipsilateral	Contralateral	Ipsilateral	Contralateral
Wire	1.4	3.6	2.3	3.3
Medtronic Lead 3389	0.8	2.3	0.2	2.0
Medtronic Lead 3387	0.3	1.2	0.2	1.0
Wire, modified trajectory	1.4	0.6	2.3	0.5

were disabled and a train of 1 ms rectangular RF pulses was transmitted using the scanner transmit body coil to achieve a better control over the characteristics of the RF exposure. To do this, the "*rf_pulse*" sequence from Siemens Service Sequence directory was used in the first level operating mode. Pulse sequence parameters are summarized in Table 3 for each experiment.

Table 4 gives the temperature rise in the gel at the tip of ipsilateral and contralateral leads during ~2.5 min RF exposure at 64 MHz and 127 MHz. As predicted by simulations, ipsilateral leads generated substantially less heating than contralateral leads. Our measurements also showed that Medtronic Lead 3389 consistently produced more heating than Lead 3387, an observation reported by other groups.

Interestingly, the modified contralateral lead trajectory with a loop at
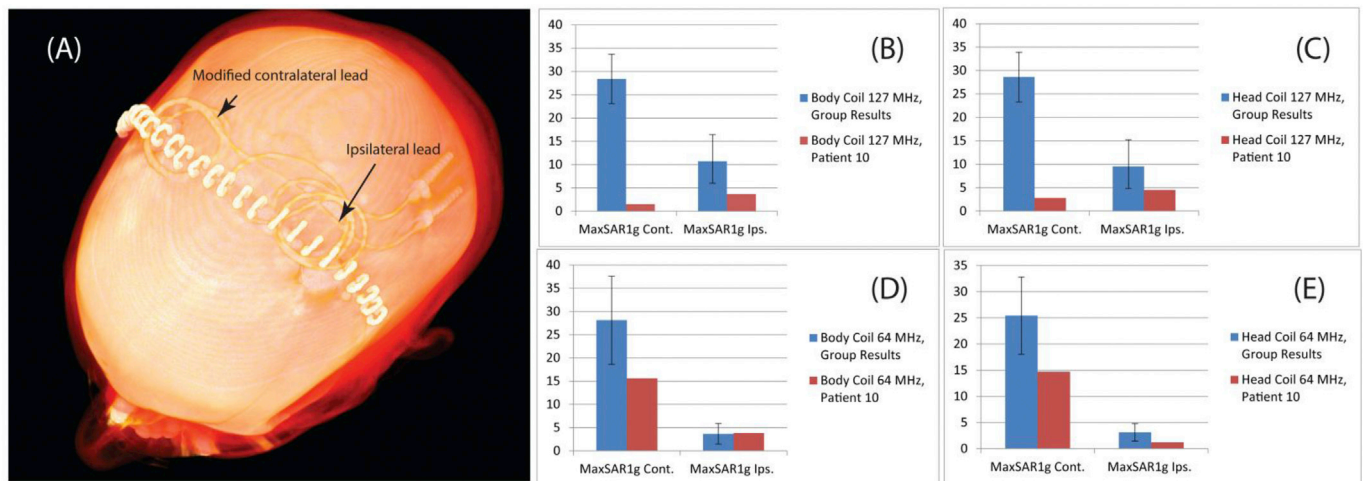
Fig. 9. (A) Postoperative CT images of a patient (Patient 10) operated using the modified lead trajectories. (B–E) Calculated *MaxSAR1g* at the tip of ipsilateral and contralateral leads of a computational model derived from Patient-10 data compared to mean *MaxSAR1g* values calculated with models derived from patients 1–9.

the burr-hole produced less heating than the ipsilateral lead. This confirms our hypothesis that modification of the lead trajectory to reduce the induced voltage along the critical portion of the lead that is exposed to the maximum tangential incident electric field also reduces the heating at the tip.

4. Modified lead trajectories: surgical feasibility and application

To explore the surgical feasibility of implementing the modifications previously described, we attempted to introduce loops in the trajectory of both ipsilateral and contralateral leads at the surgical burr-hole. To attempt to control the lead trajectory, we used curved mayo scissors passed posterior and to the left of the incision. These scissors were inserted into the opening of the blades and opened to their widest to create a pathway for a coiled lead to be inserted. We then coiled the lead upon itself in 2–3 concentric circles at the burr-hole before passing the rest of the lead toward the temporal lobe where it would be later connected to the extension. Fig. 9A shows postoperative CT images of a representative patient (Patient 10) with modified routing. Image segmentation, lead model construction and simulations were performed on Patient 10 similar to those described in previous sections patients 1–9.

Fig. 9B–E gives the simulated results of *MaxSAR1g* for Patient 10 in comparison with group analysis results of patients 1–9. At 127 MHz, the modified trajectory reduced the *MaxSAR1g* of contralateral lead by 18-folds for transmit body coil and by 10-folds for transmit head coil. At 64 MHz the modified trajectory reduced the *MaxSAR1g* of contralateral lead by 80% for both head and body coils.

5. Discussion and conclusion

Numerical modeling has been long used to understand the phenomenology of wave-tissue interaction in a wide variety of medical and diagnostic applications. Examples include use of electrostatic finite element modeling to predict the volume of activated tissue in electrical brain stimulation (Butson and McIntyre, 2006; McIntyre and Grill, 2001; Golestanirad et al., 2012a), analyzing performance of neurostimulators (Grill and Wei, 2009; Wei and Grill, 2009; Golestanirad et al., 2013), eddy current modeling to assess the distribution of cortical currents and safety of magnetic brain stimulation (Wagner et al., 2004; Wagner et al., 2004; Golestaniradet al, 2012; Golestanirad et al., 2010), analysis of body exposure to low frequency magnetic fields, and safety hazards due to motion of medical implants in magnetic fields (Golestani-Rad et al., 2007; Condon and Hadley, 2000; Golestanirad et al., 2012b). The role of numerical modeling has been also emphasized in RF safety assessment of

MRI in patients with DBS implants (U. S. Food and Drug Administration, 2015; Wilkoffet al, 2013; Angelone et al., 2010; Cabotet al, 2013; Serano et al., 2015).

The problem of RF heating of implants in MRI environment is a complex multi-variate problem with several interplaying factors. These includes the position and configuration of the implant in the body (Calcagniniet al, 2008; Nordbecket al, 2009; Matteiet al, 2008b), the anatomy of the patient and the position in the MRI coil (Nordbecket al, 2008; Nordbecket al, 2011; Golestaniradet al, 2018), and the phase of the incident RF field (Golestanirad et al., 2017; Yeung et al., 2002; Lucanoet al, 2018; Eryaman et al., 2011). Traditionally, safety assessment of active implanted medical devices (such as DBS, as well as pacemakers, and spinal cord stimulators) has been evaluated through phantom experiments employing simplified lead trajectories (Rezaiet al, 2002). In more recent years, as the large scope of parameters and complex incident field conditions has led to a significant effort in determining the incident field conditions, a four-tier approach combining numerical simulations and phantom experiments has been introduced by a joint working group of MR manufacturers, medical device manufacturers and subject matter experts. This approach is described in the ISO TS 10974 (ISO TS 10974_2018, 2017). An example illustrating the application of such approach to DBS implants has been carried on by Cabot et al. in (Cabotet al, 2013).

This work is the first attempt to apply computer modeling to cast light on the phenomenology of interaction of MRI RF fields and DBS implants in patient-specific computational models. Our results revealed a significant difference between the SAR at the tip of ipsilateral vs contralateral DBS leads in cases where both leads were routed toward the same side of the head to be later connected to one implanted IPG. Specifically, we demonstrated that the distinct routing features of ipsilateral and contralateral leads and their orientation with respect to the incident electric field are factors responsible for the difference observed in SAR and RF heating. Placement of loops right at the surgical burr-hole was shown to significantly reduce the SAR due to cancelation of the induced voltage along the initial segment of the lead, which is the part that is exposed to the maximum tangential electric field. Placement of extracranial loops has been previously suggested as a method to reduce the SAR of DBS leads (Baker et al., 2005; Golestanirad et al., 2016b), but to our knowledge this work is the first to give a detailed explanation of its mechanism of action. We also observed that placement of extracranial loops had a substantially larger effect in reducing SAR during MRI at 3 T compared to 1.5 T, which in agreement with results of previous studies (Golestanirad et al., 2016b). Finally, we demonstrated the surgical feasibility of modifying the routing of the leads without requiring

external guides and in such a way that does not add to the complexity and time of the surgery.

It is important to note however, that the current study is limited to the assessment of heating at the tips of DBS leads in isolation, i.e., prior their connection to the extension cables and the IPG, thus the results presented here should not be the extended to other configurations. Further investigation is necessary to establish the efficacy of the technique in a fully implanted system.

Another limitation of this work is that it is focused only on the RF heating of the leads due to transmit coils. Recent studies have drawn attention to the overlooked role of gradients in heating of bulk metallic implants (Zilbertiet al, 2015; Brühl et al., 2017; Zilberti et al., 2017). Simulation studies of the temperature rise induced around metallic hip prostheses by traditional, split and nunipolar gradient coils predicted a temperature rise of up to $14°C$ in the tissue depending on body's position within the gradient coil, coil's geometry, and composition of the implant (Zilbertiet al, 2015). Experiments with an acetabular cup exposed to continues trapezoidal z gradients showed up to $26°C$ temperature rise in the implant itself for the case of thermally insulated implant, and up to $3.8\ °C$ when the implant was immersed in gel. Although in these cases the tissue does not directly heat up from low-frequency induced currents of the gradient coils, its temperature could potentially rise up by conduction through the heated implant. This effect however, has been observed in bulk metallic objects, and whether or not thin wires of the leads are prone to the same effect remains to be investigated. Also in this work we used homogenous models and phantoms for simulations and experiments. The effect of tissue heterogeneity needs to be further investigated.

Future work will focus on the quantification of the SAR-reduction performance of the lead management in a cohort of patients operated using the introduced surgical technique.

Disclaimer

The mention of commercial products, their sources, or their use in connection with material reported herein is not to be construed as either an actual or implied endorsement of such products by the Department of Health and Human Services.

Acknowledgment

Appendix A. Supplementary data

Supplementary data to this article can be found online at https://doi.org/10.1016/j.neuroimage.2018.09.034.

References

Angelone, L.M., Ahveninen, J., Belliveau, J.W., Bonmassar, G., 2010. Analysis of the role of lead resistivity in specific absorption rate for deep brain stimulator leads at 3T MRI. Medical Imaging, IEEE Transactions on 29 (4), 1029–1038.

Baker, K.B., Tkach, J., Hall, J.D., Nyenhuis, J.A., Shellock, F.G., Rezai, A.R., 2005. Reduction of magnetic resonance imaging-related heating in deep brain stimulation leads using a lead management device. Neurosurgery 57 (4), 392–397.

Benabid, A.L., 2003. Deep brain stimulation for Parkinson's disease. Curr. Opin. Neurobiol. 13 (6), 696–706.

Benabid, A.L., Chabardes, S., Mitrofanis, J., Pollak, P., 2009. Deep brain stimulation of the subthalamic nucleus for the treatment of Parkinson's disease. Lancet Neurol. 8 (1), 67–81.

Blomstedt, P., Hariz, G.-M., Hariz, M.I., Koskinen, L.-O., 2007. Thalamic deep brain stimulation in the treatment of essential tremor: a long-term follow-up. Br. J. Neurosurg. 21 (5), 504–509.

Brühl, R., Ihlenfeld, A., Ittermann, B., 2017. Gradient heating of bulk metallic implants can be a safety concern in MRI. Magn. Reson. Med. 77 (5), 1739–1740.

Butson, C.R., McIntyre, C.C., 2006. Role of electrode design on the volume of tissue activated during deep brain stimulation. J. Neural. Eng. 3 (1), 1–8.

Cabot, E., et al., 2013. Evaluation of the RF heating of a generic deep brain stimulator exposed in 1.5 T magnetic resonance scanners. Bioelectromagnetics 34 (2), 104–113.

Calcagnini, G., et al., 2008. In vitro investigation of pacemaker lead heating induced by magnetic resonance imaging: role of implant geometry. J. Magn. Reson. Imag. 28 (4), 879–886.

Condon, B., Hadley, D.M., 2000. Potential MR hazard to patients with metallic heart valves: the Lenz effect. J. Magn. Reson. Imag. 12 (1), 171–176.

Elwassif, M.M., Kong, Q., Vazquez, M., Bikson, M., 2006. Bio-heat transfer model of deep brain stimulation-induced temperature changes. J. Neural. Eng. 3 (4), 306.

Eryaman, Y., Akin, B., Atalar, E., 2011. Reduction of implant RF heating through modification of transmit coil electric field. Magn. Reson. Med. 65 (5), 1305–1313.

Flora, E.D., Perera, C.L., Cameron, A.L., Maddern, G.J., 2010. Deep brain stimulation for essential tremor: a systematic review. Mov. Disord. 25 (11), 1550–1559.

Gabriel, C., Gabriel, S., Corthout, E., 1996. The dielectric properties of biological tissues: I. Literature survey. Phys. Med. Biol. 41 (11), 2231.

Gabriel, S., Lau, R., Gabriel, C., 1996. The dielectric properties of biological tissues: II. Measurements in the frequency range 10 Hz to 20 GHz. Phys. Med. Biol. 41 (11), 2251.

Golestani-Rad, L., Elahi, B., Rashed-Mohassel, J., 2007. Investigating the effects of external fields polarization on the coupling of pure magnetic waves in the human body in very low frequencies. Biomagn. Res. Technol. 5 (1), 3.

Golestanirad, L., Mattes, M., Mosig, J.R., Pollo, C., 2010. Effect of model accuracy on the result of computed current densities in the simulation of transcranial magnetic stimulation. IEEE Trans. Magn. 46 (12), 4046–4051.

Golestanirad, L., Izquierdo, A.P., Graham, S.J., Mosig, J.R., Pollo, C., 2012. Effect of realistic modeling of deep brain stimulation on the prediction of volume of activated tissue. Progress In Electromagnetics Research 126, 1–16.

Golestanirad, L., Dlala, E., Wright, G., Mosig, J.R., Graham, S.J., 2012. Comprehensive analysis of Lenz Effect on the artificial heart valves during magnetic resonance imaging. Progress In Electromagnetics Research 128, 1–17.

Golestanirad, L., Elahi, B., Molina Arribere, A., Mosig, J.R., Pollo, C., Graham, S.J., 2013. Analysis of fractal electrodes for efficient neural stimulation. Front. Neuroeng. 6 (3).

Golestanirad, L., Keil, B., Bonmassar, G., Angelone, L., Mareyam, A., Wald, L.L., 2016. Feasibility and safety of using linearly polarized rotating birdcage transmitters and closefitting receive arrays in MRI to reduce SAR in the vicinity of deep brain stimulation implants. Magn. Reson. Med. 77 (4), 1701–1712.

Golestanirad, L., Angelone, L.M., Iacono, M.I., Katnani, H., Wald, L.L., Bonmassar, G., 2016. Local SAR near deep brain stimulation (DBS) electrodes at 64 MHz and 127 MHz: a simulation study of the effect of extracranial loops. Magn. Reson. Med. 88 (4), 1558–1565.

Golestanirad, L., Keil, B., Angelone, L.M., Bonmassar, G., Mareyam, A., Wald, L.L., 2017. Feasibility of using linearly polarized rotating birdcage transmitters and close-fitting receive arrays in MRI to reduce SAR in the vicinity of deep brain simulation implants. Magn. Reson. Med. 77 (4), 1701–1712.

Golestanirad, L., et al., 2012. Combined use of transcranial magnetic stimulation and metal electrode implants: a theoretical assessment of safety considerations. Phys. Med. Biol. 57 (23), 7813.

Golestanirad, L., et al., 2017. Construction and modeling of a reconfigurable MRI coil for lowering SAR in patients with deep brain stimulation implants. Neuroimage 147, 577–588.

Golestanirad, L., et al., 2018. Changes in the specific absorption rate (SAR) of radiofrequency energy in patients with retained cardiac leads during MRI at 1.5 T and 3T. Magn. Reson. Med.

Grill, W.M., Wei, X.F., 2009. High efficiency electrodes for deep brain stimulation. In: Presented at the Annual International Conference of the IEEE Engineering in Medicine and Biology Society.

Hubble, J., Busenbark, K., Wilkinson, S., Penn, R., Lyons, K., Koller, W., 1996. Deep brain stimulation for essential tremor. Neurology 46 (4), 1150–1153.

Iacono, M.I., et al., 2015. MIDA: a multimodal imaging-based detailed anatomical model of the human head and neck. PLoS One 10 (4), e0124126.

ISO TS 10974_2018, 2017. Assessment of the Safety of Magnetic Resonance Imaging for Patients with an Active Implantable Medical Device.

Kumar, R., Dagher, A., Hutchison, W., Lang, A., Lozano, A., 1999. Globus pallidus deep brain stimulation for generalized dystonia: clinical and PET investigation. Neurology 53 (4), 871-871.

Limousin, P., et al., 1995. Effect on parkinsonian signs and symptoms of bilateral subthalamic nucleus stimulation. Lancet 345 (8942), 91–95.

Lucano, E., et al., 2018. A numerical investigation on the effect of RF coil feed variability on global and local electromagnetic field exposure in human body models at 64 MHz. Magn. Reson. Med. 79 (2), 1135–1144.

Mattei, E., et al., 2008. Complexity of MRI induced heating on metallic leads: experimental measurements of 374 configurations. Biomed. Eng. Online 7 (1), 1.

Mattei, E., et al., 2008. Complexity of MRI induced heating on metallic leads: experimental measurements of 374 configurations. Biomed. Eng. Online 7 (1), 11.

McElcheran, Clare, Golestanirad, L., Graham, S., 2014. Reduced heating of implanted electrical conductors using parallel radiofrequency transmission. In: Joint Annual Meeting of the International Society of Magnetic Resonace in Medicin. ISMRM), Milan, Italy.

McElcheran, C.E., Yang, B., Anderson, K.J., Golenstani-Rad, L., Graham, S.J., 2015. Investigation of parallel radiofrequency transmission for the reduction of heating in long conductive leads in 3 tesla magnetic resonance imaging. PLoS One 10 (8), e0134379.

McElcheran, C.E., Yang, B., Anderson, K.J., Golestanirad, L., Graham, S.J., 2017. Parallel radiofrequency transmission at 3 tesla to improve safety in bilateral implanted wires in a heterogeneous model. Magn. Reson. Med. 78 (6), 2406–2415.

McIntyre, C.C., Grill, W.M., 2001. Finite element analysis of the current-density and electric field generated by metal microelectrodes. Ann. Biomed. Eng. 29 (3), 227–235.

McIntyre, C.C., Savasta, M., Lydia, Vitek, J.L., 2004. Uncovering the mechanism(s) of action of deep brain stimulation: activation, inhibition, or both. Clin. Neurophysiol. 115 (6), 1239–1248.

McIntyre, C.C., Savasta, M., Walter, B.L., Vitek, J.L., 2004. How does deep brain stimulation work? present understanding and future questions. J. Clin. Neurophysiol. 91, 1457–1469.

Medtronic, 2017. MRI guidelines for Medtronic deep brain stimulation systems. http://manuals.medtronic.com/content/dam/emanuals/neuro/CONTRIB_228155.pdf.

Nordbeck, P., et al., 2008. Spatial distribution of RF-induced E-fields and implant heating in MRI. Magn. Reson. Med. 60 (2), 312–319.

Nordbeck, P., et al., 2009. Measuring RF-induced currents inside implants: impact of device configuration on MRI safety of cardiac pacemaker leads. Magn. Reson. Med. 61 (3), 570–578.

Nordbeck, P., et al., 2011. Impact of imaging landmark on the risk of MRI-related heating near implanted medical devices like cardiac pacemaker leads. Magn. Reson. Med. 65 (1), 44–50.

Ostrem, J.L., Starr, P.A., 2008. Treatment of dystonia with deep brain stimulation. Neurotherapeutics 5 (2), 320–330.

IEEE P1528.4™/D1.0,Recommended Practice for Determining the Peak Spatial Average Specific Absorption Rate (SAR) in the Human Body from Wireless Communications Devices, 30 MHz - 6 GHz: Requirements for Using the Finite-element Method for SAR Calculations, Specifically Involving Vehicle Mounted Antennas and Personal Wireless Devices, 2014.

Panych, L.P., Madore, B., 2018. The physics of MRI safety. J. Magn. Reson. Imag. 47 (1), 28–43.

Park, S.M., Kamondetdacha, R., Nyenhuis, J.A., 2007. Calculation of MRI-induced heating of an implanted medical lead wire with an electric field transfer function. J. Magn. Reson. Imag. 26 (5), 1278–1285.

Pavlicek, W., et al., 1983. The effects of nuclear magnetic resonance on patients with cardiac pacemakers. Radiology 147 (1), 149–153.

Rezai, A.R., et al., 2002. Neurostimulation systems for deep brain stimulation: in vitro evaluation of magnetic resonance imaging–related heating at 1.5 tesla. J. Magn. Reson. Imag. 15 (3), 241–250.

Rezai, A.R., et al., 2004. Neurostimulation system used for deep brain stimulation (DBS): MR safety issues and implications of failing to follow safety recommendations. Invest. Radiol. 39 (5), 300–303.

Rezai, A.R., et al., 2005. Is magnetic resonance imaging safe for patients with neurostimulation systems used for deep brain stimulation? Neurosurgery 57 (5), 1056–1062.

Serano, P., Angelone, L.M., Katnani, H., Eskandar, E., Bonmassar, G., 2015. A novel brain stimulation technology provides compatibility with MRI. Sci. Rep. 5.

Shellock, F.G., Fischer, L., Fieno, D.S., 2007. Cardiac pacemakers and implantable cardioverter defibrillators: in vitro magnetic resonance imaging evaluation at 1.5-tesla. J. Cardiovasc. Magn. Reson. 9 (1), 21–31.

Shrivastava, D., et al., 2010. Effect of the extracranial deep brain stimulation lead on radiofrequency heating at 9.4 Tesla (400.2 MHz). J. Magn. Reson. Imag. 32 (3), 600–607.

Sommer, T., et al., 2006. Strategy for safe performance of extrathoracic magnetic resonance imaging at 1.5 tesla in the presence of cardiac pacemakers in non–pacemaker-dependent patients a prospective study with 115 examinations. Circulation 114 (12), 1285–1292.

U. S. Food and Drug Administration, 2015. Reporting of computational modeling studies in medical device submissions -guidance for industry and food and Drug administration staff. http://www.fda.gov/downloads/MedicalDevices/DeviceRegulationandGuidance/GuidanceDocuments/UCM381813.pdf.

Vercueil, L., et al., 2001. Deep brain stimulation in the treatment of severe dystonia. J. Neurol. 248 (8), 695–700.

Wagner, T.A., Zahn, M., Grodzinsky, A.J., Pascual-leone, A., 2004. Three-dimensional head model simulation of transcranial magnetic stimulation. IEEE (Inst. Electr. Electron. Eng.) Trans. Biomed. Eng. 51 (9), 1586–1598.

Wagner, T., et al., 2004. Intracranial measurement of current densities induced by transcranial magnetic stimulation in the human brain. Neurosci. Lett. 354 (2), 91–94.

Wei, X.F., Grill, W.M., 2009. Analysis of high-perimeter planar electrodes for efficient neural stimulation. Front. Neuroeng. 2.

Wilkoff, B.L., et al., 2013. Safe magnetic resonance imaging scanning of patients with cardiac rhythm devices: a role for computer modeling. Heart Rhythm 10 (12), 1815–1821.

Yeung, C.J., Susil, R.C., Atalar, E., 2002. RF heating due to conductive wires during MRI depends on the phase distribution of the transmit field. Magn. Reson. Med. 48 (6), 1096–1098.

Zilberti, L., Arduino, A., Bottauscio, O., Chiampi, M., 2017. The underestimated role of gradient coils in MRI safety. Magn. Reson. Med. 77 (1), 13–15.

Zilberti, L., et al., 2015. Numerical prediction of temperature elevation induced around metallic hip prostheses by traditional, split, and uniplanar gradient coils. Magn. Reson. Med. 74 (1), 272–279.